Chondrule sizes within the CM carbonaceous chondrites and measurement methodologies

C. J. FLOYD [1]*, S. BENITO[2], P.-E. MARTIN[1], L. E. JENKINS[1], E. DUNHAM [3],
L. DALY [1,4,5], and M. R. LEE [1]

[1]School of Geographical and Earth Sciences, University of Glasgow, Glasgow, UK
[2]Ruhr-Universität Bochum, Chair of Materials Technology, Bochum, Germany
[3]Department of Earth, Planetary and Space Sciences, University of California, Los Angeles, Los Angeles, California, USA
[4]Australian Centre for Microscopy and Microanalysis, The University of Sydney, Sydney, New South Wales, Australia
[5]Department of Materials, University of Oxford, Oxford, UK

*Correspondence
C. J. Floyd, School of Geographical and Earth Sciences, University of Glasgow, Glasgow G12 8QQ, UK.
Email: cameron.floyd@glasgow.ac.uk

Abstract–The sizes of chondrules are a valuable tool for understanding relationships between meteorite groups and the affinity of ungrouped chondrites, documenting temporal/spatial variability in the solar nebula, and exploring the effects of parent body processing. Many of the recently reported sizes of chondrules within the CM carbonaceous chondrites differ significantly from the established literature average and are more closely comparable to those of chondrules within CO chondrites. Here, we report an updated analysis of chondrule dimensions within the CM group based on data from 1937 chondrules, obtained across a suite of CM lithologies ranging from petrologic subtypes CM2.2 to CM2.7. Our revised average CM chondrule size is 194 μm. Among the samples examined, a relationship was observed between petrologic subtype and chondrule size such that chondrule long-axis lengths are greater in the more highly aqueously altered lithologies. These findings suggest a greater similarity between the CM and CO chondrites than previously thought and support arguments for a genetic link between the two groups (i.e., the CM-CO clan). Using the 2-D and 3-D data gathered, we also apply numerous stereological corrections to examine their usefulness in correcting 2-D chondrule measurements within the CM chondrites. Alongside this analysis, we present the details of a standardized methodology for 2-D chondrule size measurement to facilitate more reliable inter-study comparisons.

INTRODUCTION

Chondritic meteorites (chondrites) are a class of primitive meteorites that are believed to have accreted during the first few million years of solar system history and so provide valuable information on the nature of the solar nebula and planetary body formation (Scott & Krot, 2013). They are composed primarily of chondrules, refractory inclusions, and fine-grained matrix material (Krot et al., 2014). Chondrites can be divided into the ordinary, enstatite, R, K, and carbonaceous classes, and further divided into 15 groups (H, L, LL, EH, EL, CI, CM, CO, CV, CK, CR, CH, CB, R, K; Weisberg et al., 2006).

Chondrules are a major component of most chondritic meteorites, with abundances ranging from 20 to 80 vol% and sizes from ∼100 μm to more than 2000 mm (Jones et al., 2000; Weisberg et al., 2006; Zanda, 2004). Chondrules are typically dominated by the Fe,Mg silicates olivine and pyroxene, with minor amounts of Fe, Ni metal and glass. Chondrule formation theories are numerous, though most agree that chondrules formed by

TABLE 1. Examples of average chondrule sizes reported for CM carbonaceous chondrites arranged in order of decreasing mean diameter.

Chondrite	Mean chondrule diameter (μm)	n	Method	Study
Murchison	558	61	XCT	Hanna and Ketcham (2018)
Asuka 12085	310	—	X-ray maps	Kimura et al. (2020)
Pollen	284	77	TLM	Kerraouch et al. (2021)
Aguas Zarcas	275	40	SEM	Kerraouch et al. (2021)
Murray	270	100	TLM	Rubin and Wasson (1986)
Maribo	268	88	TLM	Kerraouch et al. (2021)
Asuka 12169	260	—	X-ray maps	Kimura et al. (2020)
Boriskino	249	61	XCT	Kerraouch et al. (2021)
Murchison	196	—	X-ray Maps	Fendrich and Ebel (2021)
	184	—	X-ray Maps	
Jbilet Winselwan	149	321	SEM	Friend et al. (2018)
	141	187	SEM	
Reported average	270–300			

Abbreviations: SEM, scanning electron microscopy; TLM, transmitted light microscopy; XCT, x-ray computed tomography.

rapid heating and subsequent rapid cooling of a silicate precursor material (Connolly & Jones, 2016; Hewins, 1997).

Average chondrule dimensions are one aspect of chondrite classification, with distinct group-level size distributions well established (Friedrich et al., 2015; Weisberg et al., 2006). Distinct size differences of chondrules have been used to inform astrophysical theories of chondrule origin, distribution, migration, and alteration during solar system history (Cuzzi et al., 2001; Teitler et al., 2011; Wurm et al., 2010). While most chondrite groups have specific chondrule size ranges, there are some similarities between groups that have been used as evidence for potential genetic links between them (Weisberg et al., 2006). The CM (Mighei-like) and CO (Ornans-like) chondrites have been found in numerous studies to have similarly sized chondrules when compared to other chondritic groups, with reported averages of 270–300 μm (CM) and ~148 μm (CO) (Friedrich et al., 2015; Rubin & Wasson, 1986; Weisberg et al., 2006). These similarities, alongside affinities in refractory lithophile abundances and O isotopic compositions, have led to the idea of a CM-CO clan (Kallemeyn & Wasson, 1979, 1982).

The CM chondrites are a group of primitive and commonly brecciated meteorites characterized by high indigenous water contents (~9 wt% H_2O^+) acquired from their aqueously altered parent body/bodies (Bischoff et al., 2006; Hamilton et al., 2019; Jarosewich, 1990; Lentfort et al., 2020). Chondrules (including lithic clasts and mineral fragments) constitute ~20 vol% of CM chondrites, although this figure is highly variable between meteorites, and while the CM chondrule size average of 270–300 mm is well established in the literature, recent studies have reported significant deviations from this value (Table 1; Weisberg et al., 2006). Given the absence of recent detailed investigations of CM chondrule sizes and the recent range in reported averages, we present an updated analysis of CM chondrite chondrule sizes and investigate the similarities with the CO chondrite chondrules.

MATERIALS AND METHODS

During this study, 10 meteorites were examined, nine using 2-D techniques such as scanning electron microscopy (SEM) and energy-dispersive X-ray spectroscopy (EDS) mapping, and four with the 3-D technique of X-ray computed tomography (XCT). The samples analyzed and techniques used are listed in Table 2 alongside literature reported petrologic subtypes (i.e., degree of aqueous alteration), according to two classification schemes (Howard et al., 2015; Rubin et al., 2007).

2-D Chondrule Size Measurements

SEM analysis was carried out on 12 thin sections representing nine CM chondrites at the University of Glasgow's GEMS facility. A Zeiss Sigma field-emission SEM was used, with an Oxford Instruments EDS detector operated through Oxford Instruments AZtec software. An accelerating voltage of 20 kV was used for all samples. Samples were polished and coated in 20 nm of carbon prior to analysis. A total area of 750.2 mm^2 was investigated, and the sections examined are listed alongside their individual section areas and mosaic resolutions in Table 3. Backscattered electron image (BSE) mosaics and EDS maps of entire section areas were used in this study. 2-D apparent chondrule sizes were measured using the CIS method (Floyd &

TABLE 2. List of meteorite thin sections and chips investigated and their reported petrologic types and subtypes.

Meteorite	2-D analysis Section ID	3-D analysis Chip ID and Mass (g)	Petrologic type[a]	Petrologic subtype[b]
Aguas Zarcas	AZ-P1[c] (PB) AZ-P2[c] (PB)	Aguas Zarcas (3.840)[c]	—	CM2.2–2.8[d]
Cold Bokkeveld	—	BM.1727 (2.154)[e]	1.4[f]	CM2.2[g], CM2.1–2.7[h]
Kolang[c]	(TS)	—	1.3[i]	CM2.2[i]
LaPaz Icefield (LAP) 02239	5[j] (PB)	—	1.5[f]	CM2.4–2.5[k]
Lewis Cliff (LEW) 85311	90[j] (TS)	LEW85311, 84[j]	1.7[l]	CM2.6–2.7[m]
Mighei	(TS)	—	1.4[n]	—
Murchison	3.864g TS1[c] (TS) BM1970.6 (P19258)[e] (PB) BM1988, M23 (P19261)[e] (PB)	Murchison (3.86)[c]	1.5[n]	CM2.5[g], CM2.9– CM2.7 (main lithology CM2.7[h])
Paris[o]	(PB)	—	—	CM2.7–2.9[p]
Shidian[q]	(PB)	—	—	CM2.1–2.6, mainly CM2.2[r]
Winchcombe	BM.2022, M9-14 (P30552)[e] (PB)	Bag4.17 (0.025)[e] Bag4.17 Crumbs & Frag[e] Bag1_Stone34 (0.238)[e] Bag6.2_Frag2[e] Bag6.2_Frag3[e]	1.1–1.2[s]	CM2.0-2.6[t]

Abbreviations: PB, polished resin block; TS, thin section; —, not measured.
[a] Using the scheme of Howard et al. (2015).
[b] Using the scheme of Rubin et al. (2007).
[c] Commercially obtained.
[d] Kerraouch et al. (2021).
[e] Natural History Museum (U.K).
[f] Howard et al. (2015). Value from LAP 02333, which is paired with LAP 02239.
[g] Rubin et al. (2007).
[h] Lentfort et al. (2020).
[i] King et al. (2021).
[j] US Antarctic Meteorite Collection.
[k] Lee et al. (2023).
[l] Lee et al. (2019).
[m] Choe et al. (2010).
[n] Howard et al. (2015).
[o] Museum National d'Histoire Naturelle de Paris.
[p] Rubin (2015).
[q] Chinese Academy of Sciences.
[r] Fan et al. (2022).
[s] King et al. (2022).
[t] Suttle et al. (2022).

Lee, 2022) as outlined below. Samples analyzed using SEM and EDS had their petrologic subtypes determined using the Rubin (2015) classification scheme for comparison with the literature reported values. Where multiple clasts or lithologies were present, each was classified individually.

The CIS Method

The chondrule image segmentation method (CIS Method) is a simple, four-step, standardized process for 2-D chondrule size measurement and analysis taking advantage of freely available image processing and analysis software. Within the present study, only chondrules are measured; however, the CIS method would also be effective in measuring chondrule pseudomorphs present in the most heavily aqueously altered CM chondrites. The minimum chondrule size detectable using the CIS method is principally dependent on the resolution and contrast of the BSE and EDS mosaics collected, with higher resolutions allowing for a smaller minimum chondrule size to be detected. Chondrules sectioned in such a way that their diameter is smaller than the image resolution are not detected. The four steps of the CIS method are outlined below and illustrated in Figure 1.

1. *Chondrule Identification*: Whole chondrules (defined for this study later) are identified in image mosaics (in this case BSE and EDS mosaics).

TABLE 3. CM chondrite sections analyzed during this study alongside their resulting image mosaic resolution.

Meteorite	Section ID	Area (mm^2)	Resolution (µm per pixel)
Aguas Zarcas	AZ-P1	8.29	0.731
	AZ-P2	24.94	1.003
Kolang	Kolang	164.99	2.558
LAP 02239	5	79.72	1.721
LEW 85311	90	52.17	1.672
Mighei	Mighei	59.52	2.008
Murchison	3.864g_TS1	57.45	1.202
	P19258	19.39	1.203
	P19261	31.14	1.203
Paris	Paris	167.72	2.320
Shidian	Shidian	78.22	2.410
Winchcombe	P30552[a]	9.68	0.601

[a]BSE mosaic and EDS maps collected by Suttle et al. (2022).

2. *Chondrules Segmentation*: Mosaics are loaded into an image processing package; our preference was GNU Image Manipulation Program (GIMP™), where chondrules are manually segmented using the free select tool.

3. *Chondrule Measurement*: Segmented chondrules are then exported (maintaining original resolution) and imported into ImageJ, an open-source image processing package (Schindelin et al., 2012), where the scale, defined by the original resolution of the image mosaic, is set. The analyzed particle function is then used to produce and measure best-fit ellipses of each whole chondrule. Fitting an ellipse to each chondrule smooths out their often-irregular perimeter and allows ImageJ to measure maximum and minimum axes lengths perpendicular to one another (this is not possible with ferret diameter measurements). Fitting ellipses also facilitates improved comparison with XCT data analysis where fitted ellipsoids are produced.

4. *Size Analysis*: The resulting long (R_1) and short (R_3) axes lengths (mm) should subsequently be logarithmically transformed into Phi-units (φ) defined by (Equation 1) where d is in mm (Krumbein, 1936):

$$\varphi = -\log_2(d) \tag{1}$$

The transformed data in Phi-units provide equal weighting to smaller particles and allows the data to be more reliably subjected to statistical analysis such as mean, median, and standard deviation. Calculation of the mean chondrule diameter is done graphically, using Equation (2) as set out by Folk and Ward (1957) where

φ_{16} represents the average of the finest third of particles, φ_{50} the middle third and φ_{84} the coarsest third:

$$M_C = \frac{\varphi_{16+}\varphi_{50} + \varphi_{84}}{3} \tag{2}$$

Statistical analysis can be easily undertaken using GRADISTAT software (Blott & Pye, 2001) using the quarter phi interval binning. GRADISTAT also provides outputs for standard deviation, skewness, and kurtosis using the Folk and Ward (1957) graphical methods. To ensure data can be easily understood and to allow comparison to previous studies, results are reported in both φ-units and either mm or µm, for example, 2.306 φ (202 µm).

3-D Chondrule Size Measurements

Chips of five CM chondrites spanning a range of petrologic subtypes as listed in Table 4 were subjected to XCT at the University of Strathclyde, United Kingdom, using a Nikon XT H 320 LC equipped with a 180 kV transmission source. Data were corrected for beam hardening and a non-local means filter was applied post-acquisition to reduce noise. Non-local means filter settings; search window: 9, local neighbor: 4, similarity value: 0.4. Data parameters and the reconstructed voxel sizes are listed in Table 3.

Chondrules were identified within the reconstructed volume by their distinctive X-ray attenuation, appearing as dark gray objects relative to fine-grained rims (FGRs) and matrix (Hanna et al., 2015; Hanna & Ketcham, 2018). Identified chondrules were segmented in Avizo software using the method set out by Hanna et al. (2015) with chondrules manually segmented in their largest profile for each orthogonal plane (XY, XZ, & YZ). Segmented planes were subsequently exported to Blob3D, where a specialized merit function was used to fit ellipsoids to the outer margins of the segmented planes (Ketcham, 2005). Measurements of the primary and tertiary axis of each ellipsoid were recorded in Blob3D with the resulting data subjected to step 4 of the CIS method. The minimum chondrule size detectable using this technique depends on the resolution of the XCT scan with a smaller voxel size allowing smaller chondrules to be detected and measured.

Whole Chondrule Definition and Criteria

Only whole chondrules were measured in this study. For the CMs investigated, they are defined as: polymineralic, rounded edge appearance over >50% of total perimeter, surrounded by an intact FGR (not included in the measurement), not more than 50%
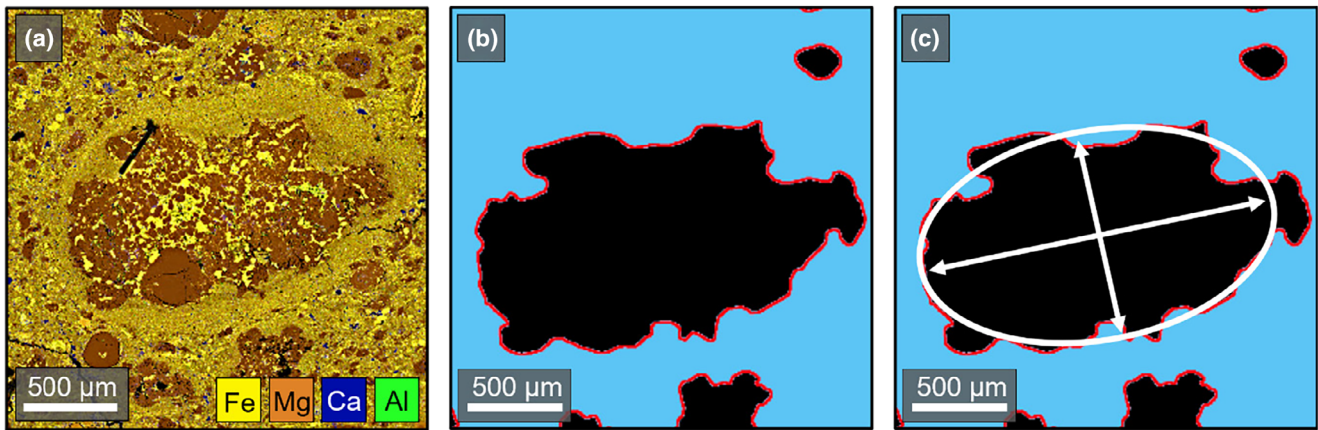
FIGURE 1. Images showing the first three steps involved in the CIS method. (a) Identification of whole chondrules by examining BSE and EDS mosaics. (b) Chondrule segmentation, involving tracing each whole chondrule in an image processor and copying it to a new image layer. (c) Chondrule measuring, involving exporting the image file containing all the segmented chondrules to ImageJ and using the "set scale" and "analyze" particles function to fit and measure ellipse dimensions.

TABLE 4. CM chondrite chips analyzed in 3-D using XCT, their scan parameters, and resulting reconstructed volume voxel resolutions. The volume given are approximate values for the chips scanned due to the general thresholding approach used.

Meteorite	Sample ID	Mass (g)	Volume (mm^3)	Accelerating voltage (kV)	Current (mA)	Number of slices	Resolution (μm per voxel)
Aguas Zarcas	Aguas Zarcas	3.84	1541	80	140	1627	12.13
Cold Bokkeveld	Cold Bokkeveld	2.15	952	70	153	2000	11.15
LEW 85311	LEW85311	0.07	34.2	65	43	2000	3.026
Murchison	Murchison	3.19	1237	90	124	2000	12.13
Winchcombe[b]	BM.2022,M3-17[a]	0.025	11.0	80	87.5	998	3.936
	BM.2022,M3-17[a]		1.67	70	85.7	996	2.130
	BM.2022,M2-34	0.238	125	130	76.9	3214	4.057
	BM.2022,M8-15[a]	0.694	1.77	70	85.7	995	2.238
	BM.2022,M8-16[a]		1.03	70	85.7	995	2.457

[a]Indicates fragments from the same parent chip (mass given of parent chip).
[b]Calculated volumes include foil wraps.

internally eroded from polishing, and not cut by a fracture or the edge of the sample. The criteria for whole chondrules have been developed based on the characteristics described in previous studies (Dodd, 1982; King & King, 1978; Metzler, 2004; Metzler et al., 1992; Weisberg et al., 2006; Wlotzka, 1983). While this definition is appropriate for defining CM chondrules for the present study, it may not be appropriate for studies of chondrules within other chondrite classes and groups.

It should also be noted that, while the majority of chondrules within the CM chondrites are encased by an FGR, there are occasional examples where this in not the case. In these instances, this definition would exclude these chondrules to preserve a consistent approach to the definition and prevent the inclusion of chondrule fragments. Additionally, the CIS technique can be used to measure pseudomorphic chondrules, although not used here.

RESULTS

2-D Analysis

A total of 983 whole chondrules were identified and measured in 2-D across 12 CM chondrite sections. Three of the sections were composed of a single lithology, while the other nine contained multiple clasts that could be distinguished by differences in elemental abundance using EDS or contrast in BSE mosaics (Figure 2; Lentfort et al., 2020). Owing to random sectioning effects, the 2-D measurements represent "apparent" chondrule size (Eisenhour, 1996) and the measurements referred to
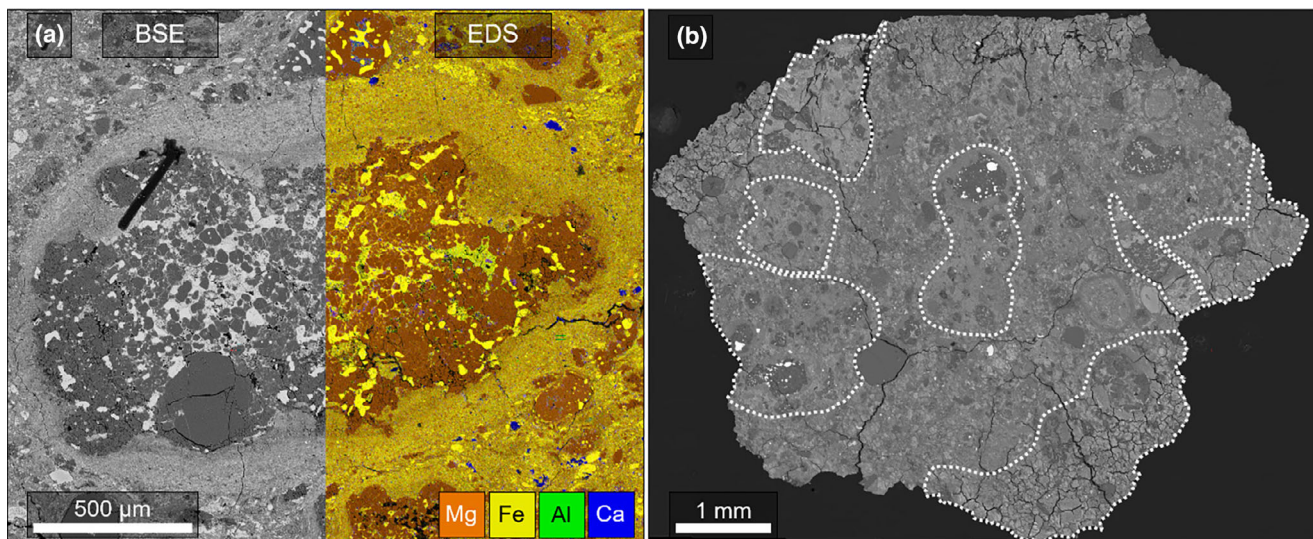
FIGURE 2. (a) A large type I chondrule, surrounded by a fine-grained rim (FGR) in Paris. (b) BSE mosaic of Aguas Zarcas section AZ_P2. The seven clasts identified within the main lithology are outlined in white.

TABLE 5. List of investigated meteorites and sections examined in 2-D using SEM. For each section the number of clasts present, whole chondrule abundance and chondrule type are reported.

	Section ID	Clasts (n)	Whole chondrules (n)	Whole chondrule Area %	Type I		Type II	
					n	(%)	N	(%)
Aguas	AZ-P1	4	9	1.23	9	100	0	0.0
Zarcas	AZ-P2	8	38	6.90	36	94.7	2	5.3
Kolang	Kolang	13	80	3.59	79	98.8	1	1.3
LAP 02239	5	5	150	10.25	144	96.0	6	4.0
LEW85311	90	3	133	10.38	127	95.5	6	4.5
Mighei	Mighei	1	30	4.65	30	100	0	0.0
Murchison	3.864g_TS1	1	140	6.98	132	94.3	8	5.7
	P19258	7	10	2.80	9	90.0	1	10.0
	P19261	4	50	4.06	48	96.0	2	4.0
Paris	Paris	5	215	7.80	207	96.3	8	3.7
Shidian	Shidian	1	90	8.30	89	98.9	1	1.1
Winchcombe	P30552	1	38	7.21	38	100	0	0.0
Total		53	983		948	96.4	35	3.6

hereafter reference the lengths of either the major (R_1) or minor (R_3) axes of the best-fit ellipses produced.

Chondrule Types and Abundances

During chondrule characterization, the relative abundances of type I (FeO-poor and volatile poor) and type II (FeO-rich) chondrules (Hewins, 1997) were noted alongside the areal. % of whole chondrules (Table 5). Results indicate that the relative abundance of type I and II chondrules is broadly consistent with previous studies (Hewins et al., 2014). The areal % of whole chondrules is highly variable between the whole polished sections examined supporting the findings of Weisberg et al. (2006);

there is no relationship between areal. % of chondrules and average R_1 diameter within each polished section. Chondrule abundances differ between the clasts and lithologies as can be observed in Figure 2b supporting previous observations of chondrule-rich and chondrule-poor lithologies (Suttle et al., 2022).

2-D Size Distributions

Prior to logarithmic transformation, the 2-D size data exhibited a significant positive skew that could be approximately characterized as log-normal, supporting the approximately log-normal distribution found by Friend et al. (2018). Following conversion into Phi-units,
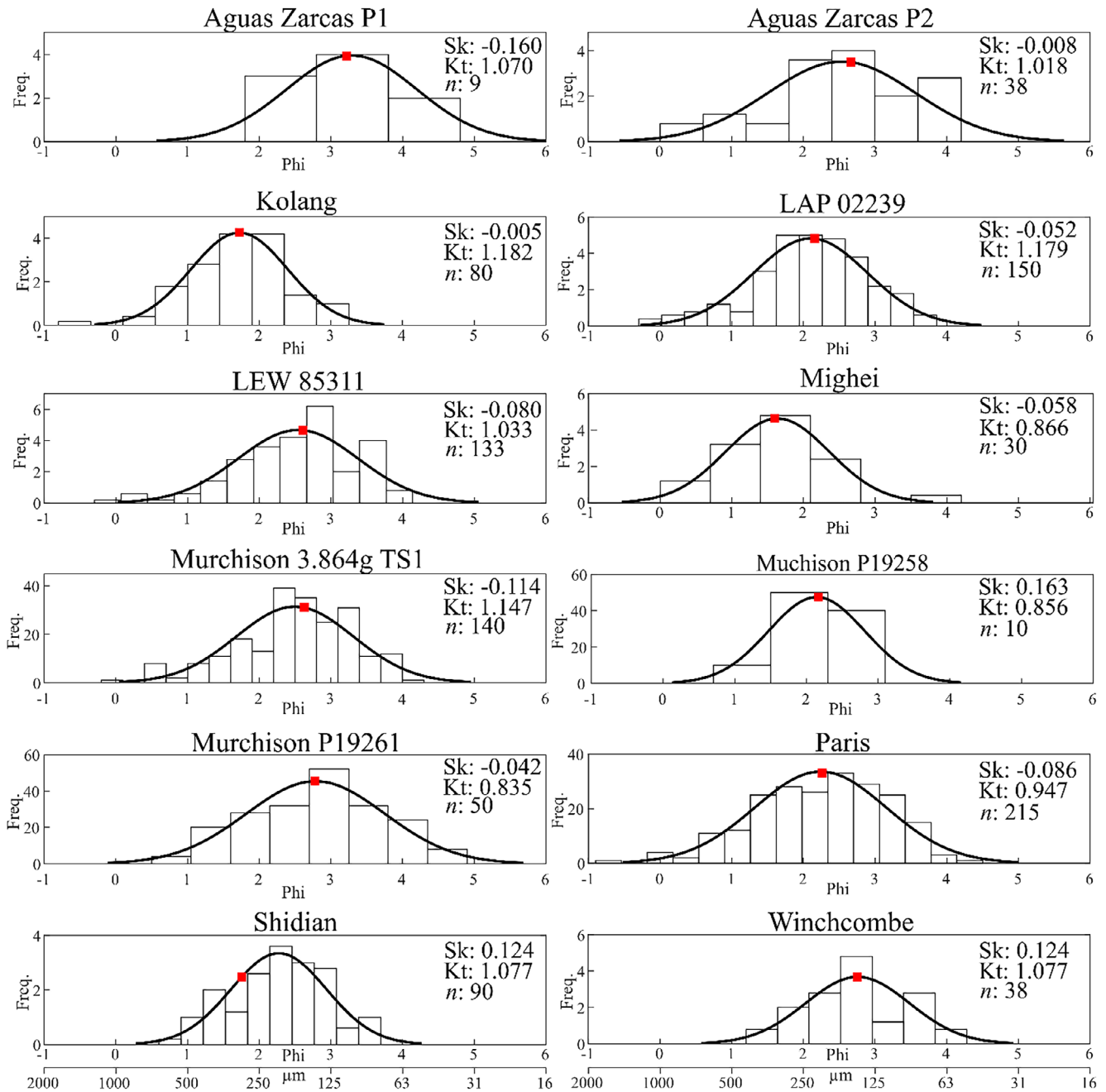
FIGURE 3. Histograms for chondrule size in Phi-units for each of the polished sections examined. Black lines indicate fitted normal distribution curves and the red squares indicate the average chondrules sizes for the sections as calculated using the CIS method. Values for kurtosis (Kt), skewness (Sk), and number of chondrule (n) are stated in the top right of each histogram.

chondrule size histograms were produced for each section and are reported alongside associated skewness and kurtosis values (Figure 3). After logarithmic transformation, chondrules exhibit approximately normal distributions. Inter-clast variations in size are observed, with notable differences between the clasts of Paris, Aguas Zarcas AZ-P2, and Kolang.

The host clasts or lithologies of chondrules were assigned a petrologic subtype (Table 6), and results reveal size distributions generally symmetrical within lithologies of subtypes CM2.2, 2.4, and 2.5. A marginal coarse skew (0.113) was observed in size distributions of CM2.7 lithologies. Kurtosis values indicate mesokurtic distributions for CM2.2, 2.4, and 2.7 and a leptokurtic

C. J. Floyd et al.

TABLE 6. 2-D "apparent" chondrule sizes and statistics for major and minor axis of all chondrule-bearing clasts and lithologies within each section.

Polished section	Clast (C_x)	n	Petrological subtype	Average R_1 ϕ (µm)	σ	Median R_1 ϕ (µm)	Average R_3 ϕ (µm)	σ	Average aspect ratio
Aguas Zarcas AGZ_P1	C_1	7	2.2	3.214 (107.8)	0.62	3.415 (93.8)	3.531 (86.52)	0.55	1.24
	C_2	2	2.2	2.917 (132.4)	1.27	2.000 (250.0)	3.493 (88.81)	1.07	1.42
	Total	9	2.2	3.216 (107.6)	0.97	3.415 (93.8)	3.528 (86.70)	0.88	1.28
Aguas Zarcas AGZ_P2	C_1	2	2.3	2.576 (167.7)	0.86	2.000 (250.0)	2.982 (126.6)	0.76	1.23
	C_2	6	2.3	3.487 (89.31)	0.46	3.474 (90.0)	3.831 (70.25)	0.66	1.29
	C_3	8	2.3	2.510 (175.6)	0.81	2.395 (190.1)	2.787 (144.9)	0.62	1.34
	C_4	5	2.3	2.092 (234.5)	0.78	2.540 (171.9)	2.562 (169.3)	0.91	1.37
	C_5	2	2.2	1.155 (449.1)	0.96	1.468 (3615)	1.661 (316.2)	0.96	1.46
	C_6	1	2.2	3.899 (0.067)	—	—	4.083 (0.059)	—	1.14
	C_7	14	2.2	2.452 (182.8)	1.07	2.159 (223.9)	2.866 (137.3)	1.01	1.36
	Total	38	—	2.666 (157.5)	1.07	2.579 (167.4)	1.031 (122.3)	0.98	1.34
Kolang	C_1	26	2.2	1.812 (284.9)	0.74	1.850 (277.5)	2.343 (197.1)	0.56	1.48
	C_2	15	2.2	1.861 (275.4)	0.61	1.868 (273.9)	2.282 (205.6)	0.45	1.42
	C_3	1	2.2	1.577 (335.0)	—	—	1.756 (296.0)	—	1.13
	C_4	22	2.2	1.536 (345.0)	0.69	1.456 (364.5)	2.126 (229.1)	0.75	1.46
	C_5	1	2.2	1.296 (407.0)	—	—	1.34 (395.0)	—	1.03
	C_6	6	2.2	1.536 (344.9)	0.49	1.494 (355.0)	1.862 (275.1)	0.49	1.32
	C_7	1	2.2	1.442 (368.0)	—	—	1.595 (331.0)	—	1.11
	C_8	1	2.2	3.070 (119.0)	—	—	3.293 (102.0)	—	1.17
	C_9	7	2.2	1.720 (303.5)	0.32	1.676 (312.9)	2.304 (202.4)	0.41	1.58
	Total	80	2.2	1.722 (303.0)	0.67	1.737 (300.0)	2.221 (214.5)	0.60	1.44
LAP 02239, 5	C_1	1	2.5	1.847 (0.278)	—	—	2.139 (0.227)	—	1.22
	C_2	92	2.4	2.267 (207.8)	0.80	2.238 (212.0)	2.708 (153.0)	0.82	1.45
	C_3	4	2.5	1.909 (266.2)	0.91	1.737 (300.0)	2.323 (199.8)	0.91	1.53
	C_4	53	2.5	2.001 (249.8)	0.75	2.020 (246.6)	2.443 (183.9)	0.68	1.42
	Total	150	—	2.157 (224.2)	0.81	2.140 (226.9)	2.603 (164.6)	0.78	1.44
LEW 85311, 90	C_1	118	2.7	2.623 (162.4)	0.84	2.605 (164.3)	3.001 (124.9)	0.82	1.36
	C_2	12	2.7	2.584 (166.8)	0.74	2.737 (150.0)	2.912 (132.8)	0.76	1.27
	C_3	3	2.7	2.605 (164.3)	0.08	2.605 (164.3)	2.953 (129.2)	0.15	1.19
	Total	133	2.7	2.606 (164.2)	0.82	2.605 (164.3)	2.994 (125.6)	0.80	1.35
Mighei	—	30	2.2	1.599 (330.2)	0.66	1.640 (320.9)	2.020 (246.6)	0.72	1.34
Murchison 3.864g TS1	—	140	2.2	2.628 (161.8)	0.79	2.657 (158.5)	3.178 (110.5)	0.77	1.43
Murchison P19258	C_1	9	2.5	2.144 (226.3)	0.64	1.956 (257.7)	2.465 (181.2)	0.71	1.23
	C_2	1	2.2	2.204 (217.0)	—	—	2.900 (134.0)	—	1.62
	Total	10	—	2.752 (222.7)	0.62	2.000 (250.0)	2.515 (175.3)	0.70	1.27
Murchison P19261	C_1	27	2.5	2.461 (181.6)	0.94	2.415 (187.5)	2.826 (141.0)	0.90	1.47
	C_2	17	2.2	3.419 (93.51)	0.85	3.540 (85.99)	3.685 (77.74)	0.87	1.27
	C_3	4	2.2	3.324 (99.89)	0.41	3.238 (106.0)	3.530 (86.59)	0.51	1.27
	C_4	2	2.5	2.158 (224.1)	0.35	2.247 (210.1)	2.650 (159.4)	0.36	1.50
	Total	50	—	2.779 (145.6)	1.00	2.825 (141.2)	3.276 (103.2)	0.93	1.39
Paris	C_1	165	2.7	2.293 (204.1)	0.93	2.336 (198.1)	2.777 (145.9)	0.96	1.45
	C_2	25	2.7	2.327 (199.3)	0.93	2.415 (187.5)	2.660 (158.2)	0.91	1.46
	C_3	9	2.7	2.368 (193.8)	0.86	1.967 (255.8)	3.115 (115.5)	0.76	1.71
	C_4	9	2.7	1.968 (255.6)	094	1.616 (326.2)	2.449 (183.2)	0.95	1.40
	C_5	7	2.7	2.262 (208.5)	0.97	2.415 (187.5)	2.869 (136.9)	0.97	1.49
	Total	215	2.7	2.259 (209.0)	0.93	2.311 (201.5)	2.757 (148.0)	0.96	1.46
Shidian	—	90	2.2	1.758 (295.6)	0.73	1.685 (311.0)	2.243 (211.3)	0.71	1.46
Winchcombe	—	38	2.2	2.752 (148.5)	0.81	2.662 (158.0)	3.257 (104.6)	0.70	1.45

Abbreviations: n, number of chondrules measured; σ, one SD.

TABLE 7. Chondrule size statistics for lithologies classified by petrologic subtype (where $n > 10$). Graphical statistical analysis based on Folk and Ward (1957). A figure showing the negative correlation between petrologic subtype and the Weighted Average R_1 is provided in the Figure S1.

Petrologic subtype	Weighted average R_1 ɸ (μm)	Graphical skewness (ɸ)	Graphical kurtosis (ɸ)
CM2.2	2.154 (224.69)	0.001	1.001
CM2.4	2.267 (207.80)	−0.033	1.085
CM2.5	2.454 (182.40)	−0.027	1.147
CM2.7	2.419 (186.95)	−0.113	1.032

distribution for CM2.5. A Kolmogorov–Smirnov two sample one-tailed statistical test was conducted to investigate the differences in average chondrule size between petrologic subtypes. This nonparametric test compares two distributions and does not assume normality. Clasts or lithologies with a small sample size ($n < 10$ chondrules) were removed from this analysis as it was judged these could introduce error by being unrepresentative. The results of the Kolmogorov–Smirnov test indicate that, at a 97% confidence interval (CI), chondrules from the CM2.7 population are smaller than those in the CM2.2 population. Additionally, CM2.7 chondrules are smaller than chondrules in CM2.4 with 90% confidence interval. No relationship was observed between chondrule aspect ratio and petrologic subtype or axis size. To account for the presence of chondrule-rich lithologies within some samples and the spread of data within the CM2.2 classification, weighted averages were calculated for clasts or lithologies with $n > 10$ chondrules. Weighted averages indicate a minor negative correlation between chondrule R_1 length and the extent of aqueous processing (Table 7).

3-D Analysis

A total of 954 chondrules were identified and measured in 3-D within nine CM chondrite chips (Table 8). Where possible, all identifiable chondrules within a clast or lithology were segmented. However, given the time-consuming nature of 3-D segmentation, for larger volumes where segmentation of all chondrules would have been impractical, a minimum of 100 chondrules were segmented per chip/clast. Within some volumes, multiple clasts could be clearly distinguished by differences in X-ray attenuation. However, due to the often-small sizes and similarities in attenuation coefficients, constraining lithological boundaries was challenging. Consequently, the study of lithological variations was limited to Aguas Zarcas and Winchcombe Bag 1 Stone 34; in those samples, the

different clasts could be confidently identified by their contrasts in attenuation coefficients and were large enough to obtain a significant number of chondrule measurements. For all other meteorites, chondrules were segmented from the dominant lithology present. The appearance of chondrules within the different scan volumes was heavily dependent on scan resolution with resolutions greater than 3–4 μm per voxel allowing improved distinction and thus characterization and measurement of smaller chondrules, more finely crystalline materials such as FGRs, and inter-chondrule Fe,Ni metal (Figure 4). The 3-D measurements collected represent "true" chondrule size and the chondrule sizes referred to hereafter reference the lengths of the long or short axes of best-fit ellipsoids.

3-D Size Distributions

Size distribution histograms are in Figure 5 alongside fitted normal distribution curves and skewness and kurtosis values with statistical data in Table 8. In common with the 2-D data sets, the 3-D skewness and kurtosis values have a generally symmetrical distribution once logarithmically transformed. Average sizes are generally larger than those recorded in 2-D with a greater range of values documented. A correlation between average R_1 and scan resolution is also observed. Aguas Zarcas, Cold Bokkeveld, and Murchison samples were scanned at the coarsest resolutions and were observed to have significantly larger R_1 lengths. There are subtle contrasts in sizes between clasts, although the extent of these differences appears less pronounced compared to 2-D. Average chondrule aspect ratios were strikingly similar between all 3-D analyses, with values ranging from 1.57 to 1.77.

2-D–3-D Size Corrections

Reconciling the effects of random sectioning and the relationship between 2-D "apparent" and 3-D "true" particle size has been previously explored in numerous previous studies (Benito et al., 2019; Cuzzi & Olson, 2017; Eisenhour, 1996; Metzler, 2018; Sahagian & Proussevitch, 1998). Many of these authors have developed stereological correction models to predict 3-D particle size distributions based on 2-D apparent diameters, several which have been applied to the study of chondrule sizes (Benito et al., 2019; Cuzzi & Olson, 2017; Eisenhour, 1996).

Many of the stereological corrections applied are based on the assumption that particles can be approximated by spheres and that reconciling their 3-D size can be reduced to four effects (Benito et al., 2019):

i. A randomly cut sphere is likely to be non-diametrical and therefore not represent a cross section through the widest point of a sphere.

TABLE 8. 3-D "true" chondrule sizes and statistics for major and minor axes of chondrule-bearing clasts and lithologies examined within each chip.

Sample	Clast (C_x)	n	Average R_1 ɸ (µm)	σ	Median R_1 ɸ (µm)	Average R_3 ɸ (µm)	σ	Average aspect ratio
Aguas Zarcas	C_1	102	1.449 (366.3)	0.62	1.494 (355.0)	2.175 (221.5)	0.55	1.72
	C_2	104	1.545 (342.8)	0.40	1.552 (341.1)	2.201 (217.4)	0.41	1.57
	C_3	107	1.410 (376.3)	0.46	1.399 (379.1)	2.196 (218.2)	0.42	1.77
	Total	313	1.474 (360.1)	0.49	1.476 (259.5)	2.206 (216.7)	0.46	1.69
Cold Bokkeveld	—	103	1.164 (446.1)	0.47	2.507 (175.9)	1.780 (291.1)	0.48	1.57
LEW 85311	—	154	2.565 (169.0)	0.59	2.575 (167.8)	3.184 (110.0)	0.51	1.60
Murchison 3.864g	—	180	1.106 (464.5)	0.58	1.163 (446.6)	1.811 (285.1)	0.52	1.69
Winchcombe								
BM.2022,M2-34	C_1	30	2.427 (186.0)	0.57	2.427 (186.0)	3.093 (117.2)	0.51	1.62
	C_2	50	2.170 (222.1)	0.51	2.143 (226.5)	2.857 (138.1)	0.45	1.68
BM.2022,M3-17	—	40	2.320 (200.3)	0.59	2.435 (185.0)	2.962 (128.4)	0.60	1.62
BM.2022,M3-17	—	30	3.159 (111.9)	0.62	3.102 (116.5)	3.811 (71.26)	0.56	1.70
BM.2022,M8-15	—	31	2.706 (153.3)	0.71	2.803 (143.3)	3.487 (89.16)	0.64	1.68
BM.2022,M8-16	—	23	2.712 (152.6)	0.57	2.793 (144.3)	3.361 (97.30)	0.56	1.61
Total	—	204	2.501 (176.7)	0.69	2.507 (175.9)	3.201 (108.7)	0.66	1.66

Abbreviations: n, number of chondrules measured; σ, one SD.
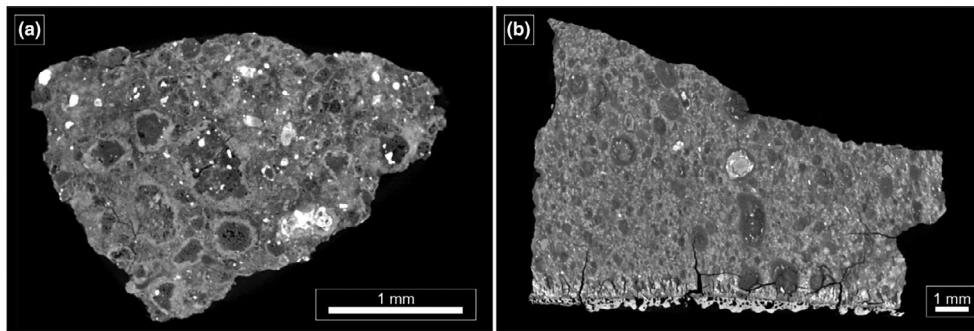
FIGURE 4. Example XCT slices showing dark objects identified as chondrules and the differences in resolution between some volumes. (a) XCT slice of LEW 85311 (resolution: 3.026 µm per voxel). Within this volume, fine-grained rims and intra-chondrule Fe,Ni metal grains can be easily identified. (b) XCT Slice of Murchison 3.864g within which the fine-grained rims and Fe,Ni metal grains are less well resolved even accounting for its lower magnification (resolution: 12.13 µm per voxel).

ii. Larger spheres will be more frequently sectioned and measured in 2-D due to their larger diameters.
iii. Thin sections themselves have a dedicated thickness (in the case of petrographic thin sections typically 30 µm).
iv. Sections cutting a sphere in a plane slightly smaller than that of the sphere radius may be missed due to the resolution of the measuring method.

Four stereological corrections, outlined briefly below, were applied to the 2-D data set Murchison 3.864g TS1 and compared with the XCT data set Murchison 3.864g, from which the thin section was made. Although the data sets are not precisely correlated, they provide an opportunity to compare, for the first time, the outcomes of such stereology models with real 2-D and 3-D data

from a meteorite. The outcomes of the corrections are shown in Figure 6.

Eisenhour (1996): The first model developed and applied specifically to chondrule size analysis (developed using CO chondrite chondrules) is based on effects (i), (ii), and (iii) listed above and assumes chondrules as undeformed spheres. The original findings of this model indicated that the corrected chondrule sizes have mean/median values smaller than those of the apparent diameters measured in 2-D, there is an increase in the number of minimum diameter chondrules recorded, and the data are transformed from having a nearly log-normal distribution to conforming to a Weibull probability function.
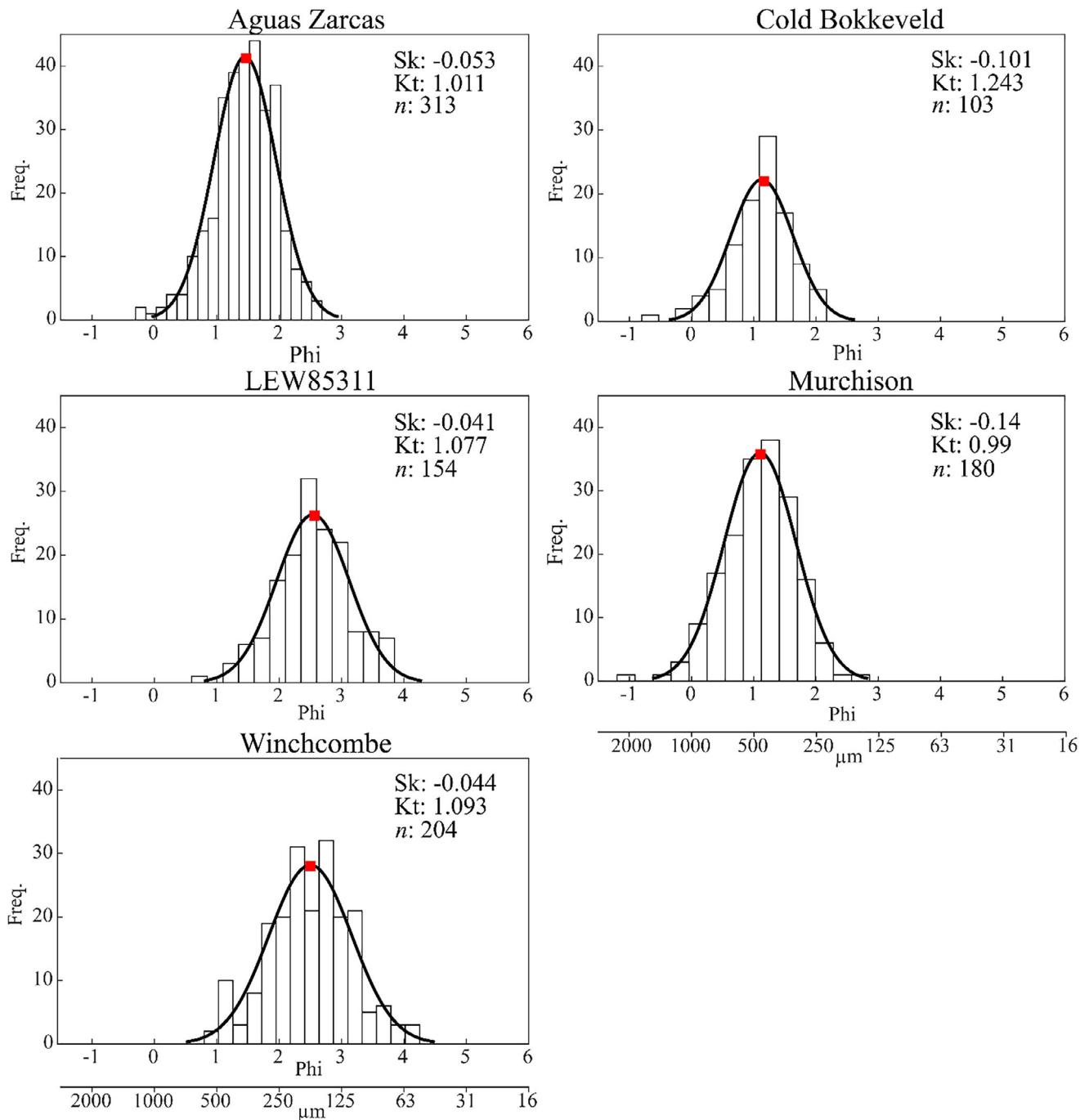
FIGURE 5. Histograms of major axis chondrule sizes in Phi-units for chondrules in each of the meteorites examined by XCT. Black lines indicate fitted normal distribution curves and the red squares indicate the graphical average chondrules sizes as calculated using the analysis component of the CIS method. Values for kurtosis (Kt), skewness (Sk), and number of chondrules (n) are in the top right of each histogram.

Sahagian and Proussevitch (1998) were originally developed to examine vesicles sizes in basalts, this model addresses the assumption of particle sphericity. Three systems are defined within this model to help users understand this issue: (a) monodispersal systems, where particles are the same size and shape; (b) polydispersal systems, where particles are the same shape but different sizes; (c) multidispersal systems, where particles have different sizes and shapes. The Sahagain and Proussevitch model uses individual particle areas and aspect ratios to
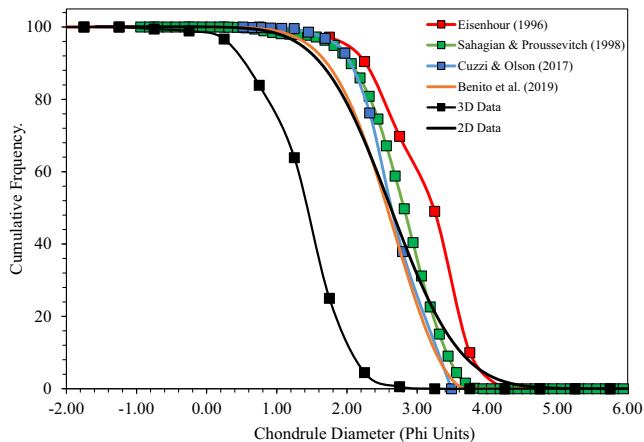
FIGURE 6. Cumulative frequency diagram comparing the outcomes of the Eisenhour (1996), Sahagian and Proussevitch (1998), Cuzzi and Olson (2017), and Benito et al. (2019) particle size correction models. Corrections were carried out on the 2-D data collected from Murchison 3.864g TS1. Also shown are the 3-D data collected from chip Murchison 3.864g, which is plotted at half-φ intervals. The figure shows a lack of correlation between the 2-D corrected and 3-D data. As will be discussed in the following sections, this is a consequence of the XCT resolution used for analysis.

produce a size correction based on the assumption of a multidispersal system.

Cuzzi and Olson (2017): This is the second dedicated model developed to investigate particle size corrections in chondrites. In common with Eisenhour (1996), this model assumes particle sphericity (therefore categorizing itself as a polydispersal model) and zero-thickness slicing. The presented algorithms are based on an inversion technique which "unfolds" arithmetically or geometrically binned histograms of particle apparent diameters in 2-D sections. Due to the discrete nature of the recovery process, the model requires a minimum of 100–300 apparent diameter measurements to produce a good recovery.

Benito et al. (2019): This is a refinement on the Cuzzi and Olson (2017) model. To address the main shortcomings of the original method, namely scatter in the recovered distribution and negative-valued histogram bins, Benito et al. proposed a fitting step and the inclusion of numerical optimization tools to solve the inverse problem. An additional benefit of this model is a reduction in the minimum number of measurements required (50–100) to produce a good reconstruction.

Examining a cumulative distribution function (CDF) plot of the four models (Figure 6) reveals subtle differences between model outcomes. The Eisenhour model plots almost entirely to the right of the 2-D data indicating a model outcome predicting smaller chondrule sizes. The Sahagian & Proussevitch and Cuzzi & Olson models are similar to one another, although the former predicts a

median reconstructed diameter smaller than the apparent measured diameter while the Cuzzi & Olson model matches closely with the 2-D measured data. Finally, the Benito model predicts a reconstructed chondrule diameter which is generally to the left of the 2-D plotted data and indicates a larger reconstructed diameter than the measured apparent diameters.

It is worth noting that the Cuzzi & Olson and the Benito reconstructions were performed on the original log-normally distributed measurements as opposed to the Phi-transformed data. These models predict the 3-D size distribution that would produce the observed 2-D distribution by assessing the cumulative contributions of all measured cross-sectional areas. The transformation proposed in Equation (1) crucially interferes with this recovery process. As a result, the Phi transformation was performed on the reconstructed PDFs.

DISCUSSION

Measurement of 1937 CM chondrules suggests a significant discrepancy between results from 2-D and 3-D measuring methods alongside variations in model outcomes when applying different stereological corrections. Below we evaluate these measuring methodologies, stereological corrections provide an updated summary of the CM chondrule sizes and discuss the implications for the putative CM-CO clan.

2-D versus 3-D Methodologies

The data reported here illustrate the complexities accompanying what initially appears to be a simple task of determining average chondrule size. The reported average values show significant differences between the two measurement techniques used, with 3-D "true" chondrule diameters spanning a far greater range of average values than the 2-D "apparent" measurements. This discrepancy is best illustrated by comparing the measurements recorded for Murchison and Aguas Zarcas, which both report 3-D average R_1 values of more than 1.515 φ (350 μm), far in excess of the maximum total R_1 averages reported for these chondrites using 2-D methods (2.752 φ [222.7 μm] and 2.666 φ [157.5 μm], respectively). The larger R_1 values recorded in 3-D are similar to those observed by Hanna et al. (2015) from a different Murchison chip and taken together could suggest 2-D measurements are significantly underestimating the "true" chondrule size. However, the XCT scan resolutions used in these studies are more than 10 μm per voxel, making identification and accurate segmentation of smaller chondrules (<~100 μm) challenging. The positive skew towards finer particles within all the 2-D chondrule size data sets indicates a significant portion of smaller chondrules are being overlooked in 3-D studies due to
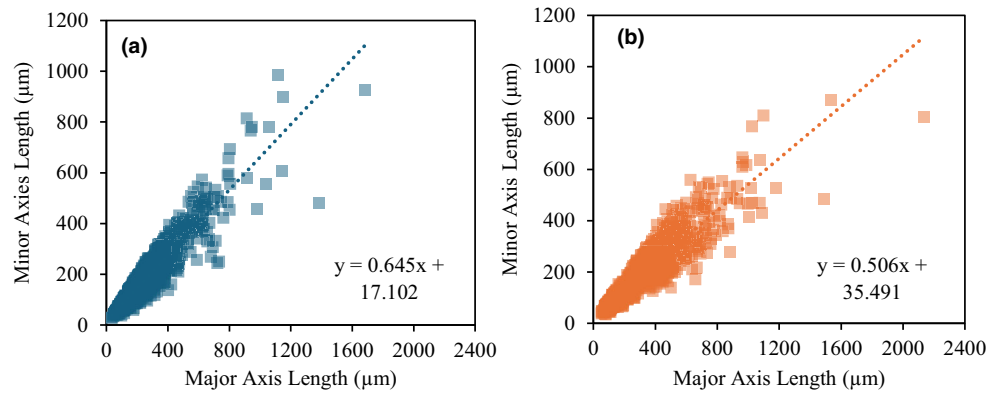
FIGURE 7. Major/minor axis relationships for all 2-D measurements $n = 983$ (a) and all 3-D measurements $n = 954$ (b).

insufficient scan resolutions. The 3-D data sets for Winchcombe and LEW 85311 highlight this bias. In these scans, a reconstructed voxel size of $<4\,\mu m$ was achieved, and the average 3-D values recorded are much more comparable to those collected using the 2-D methods with a resolution of ~2–$4\,\mu m$ per pixel (Tables 4, 6 and 8).

The use of XCT to accurately measure the sizes of objects within CM chondrites therefore appears to be highly resolution dependent, with the potential for resolution-induced bias toward larger chondrules at poor scan resolutions. The comparable nature of high-resolution scans ($4\,\mu m$ per voxel or better) and the 2-D measurements from the same chondrites provide confidence that the high-resolution scans are producing a more accurate indication of chondrule sizes compared to those scans at coarser resolution. As a result of this finding, it is proposed that scan resolutions of $\sim4\,\mu m$ per voxel (or better) are required for accurate determination of 3-D "true" chondrule sizes by XCT. Thus, XCT data sets with resolutions $>4\,\mu m$ per voxel are excluded from determination of CM averages in this study.

Stereology Corrections

The different stereological corrections illustrated in Figure 6 demonstrate the range in outcomes that can be achieved by applying different models. The most significant difference was observed when the Eisenhour (1996) model was applied. The outcome of the Eisenhour (1996) model predicts 3-D chondrule sizes smaller than those measured in 2-D, implying that random 2-D sectioning is producing an overestimate of the "true" chondrule size. While this finding is consistent with the outcome of the model when published, it disagrees with the 3-D measured data and the logical expected result given the probability of randomly sectioning only the largest diameters of chondrules.

The Sahagian & Proussevitch model fared slightly better, producing a model outcome more akin to the 2-D

data. Despite a median value below that of the 2-D measured data, the Sahagian & Proussevitch model did predict $\sim20\%$ of chondrules were likely to be larger than measured in 2-D. Given the model's focus on dealing with non-spherical components and multidispersal systems, it perhaps surprising that this model does not better reflect the larger chondrule sizes indicated by the 3-D analysis (Figure 7).

The Cuzzi & Olson model has similarities to both the Sahagian & Proussevitch and Benito et al. models. Its similarities to the Benito model are unsurprising given their comparable methodology. The deviation from the Benito model can likely be explained by the improvements in the Benito reconstruction. Figure 8 illustrates the differences between the Cuzzi & Olson and Benito models in more detail by comparing the outcomes as both probability density functions (PDFs) and CDFs. This comparison highlights the smoothing effect the Benito model has as a result of the underlying data fitting step. Furthermore, the Benito model is the only one to produce a reconstructed median size larger than that measured in 2-D, and therefore agrees with the general findings of the 3-D "true" measured diameters.

There remains a significant discrepancy between the four model outcomes and the 2-D/3-D data collected. We suggest two possible factors that may be responsible for this:

1. With the exception of Sahagian & Proussevitch, all models have assumed chondrule sphericity. The chondrule dimensions and aspect ratios measured in 2-D and 3-D demonstrate that CM chondrite chondrules are inherently non-spherical and therefore any assumption of sphericity is misplaced. It is suggested that a combination of pre-accretionary and post-accretionary processes are responsible for chondrule shape (Charles et al., 2018; Miura et al., 2008; Tsuchiyama et al., 2003) with post-accretionary
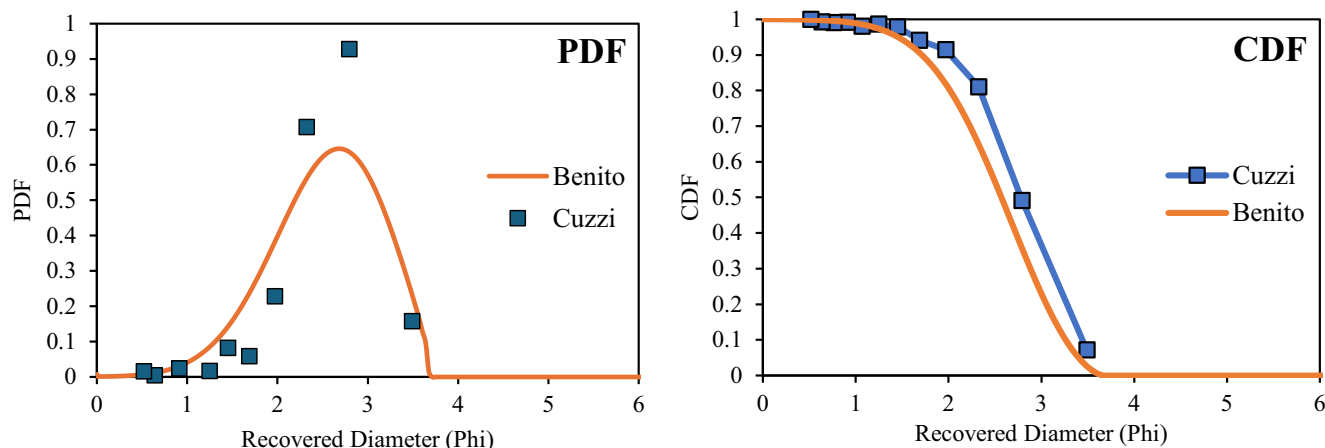
FIGURE 8. PDF and CDF plots comparing the Cuzzi and Olson (2017) and Benito et al. (2019) models shown in blue and orange, respectively. The PDF plot reveals the extent to which the Benito et al.'s model produces a smoother fit compared to the Cuzzi & Olson model; this significant smoothing is not noticeable in the CDF diagram.

processes being particularly important for CM chondrites (Lindgren et al., 2015; Rubin, 2012; Vacher et al., 2018). While it is difficult to quantify the effects of this assumption on the model outcomes, the consequences of non-sphericity on stereological models which assume sphericity has been widely discussed within the stereological literature and is likely to be having some effect on the model outcomes (Cuzzi & Olson, 2017; Oakeshott & Edwards, 1992; Sahagian & Proussevitch, 1998).

2. The relatively poor resolution of the 3-D Murchison data used here (12.13 μm per voxel) compared to the 2-D Murchison data (1.202 μm per pixel). Such disparity between the 2-D and 3-D data resolutions is likely leading to an exaggerated difference between the 3-D and 2-D data curves. It is unlikely that using a similar resolution for 2-D and 3-D analyses will produce a 3-D "true" diameter smaller than that recorded in 2-D diameters however, it may significantly reduce the difference between the two and allow for better comparison with the models.

None of the models used produced a correction which aligns with the 3-D measured true diameters, and this is likely a consequence of both factors listed above. However, given the Benito model is the only one to produce a reconstruction suggesting an increase in the number of larger chondrules, we propose the Benito model is likely the most accurate model currently available for reconstructing 3-D chondrule diameters. An updated version of the Benito et al. (2019) code, designed to produce outcomes in Phi-units, is provided in Supplement 1. Future analysis using higher resolution XCT data will help build further understanding of the accuracy of the Benito model to true chondrule diameters.

Comparison with Chondrule Size Data in the Literature

A comparison of the data presented here (Figure 9) with literature values indicates that the stated 270–300 μm average for CM chondrules (Friedrich et al., 2015; Rubin & Wasson, 1986; Weisberg et al., 2006) is an overestimate. This conclusion supports other recent findings of individual CM chondrites, where methodologies similar to those used here, have yielded smaller than reported chondrule sizes (Fendrich & Ebel, 2021; Friend et al., 2018). An average CM chondrule size of 2.363ϕ (194 μm) is likely a more appropriate estimate when analysis involves SEM and higher resolution XCT techniques (i.e., a 28% reduction compared to 270 μm). The high-resolution imaging and segmentation techniques, alongside the improved statistical methodology, are likely responsible for this reduction in average. A comparison of the CIS methodology with simple arithmetic averaging of non-logarithmically transformed (and thus non-Gaussian data) shows that average values are 8.3%–28% smaller when analyzed using the CIS methodology.

Comparing average values across the literature is inherently challenging given the variety of methodologies used. Given the ease and effectiveness of CIS methodology, we suggest it could be adopted as a standardized approach for chondrule measurement. Such standardization would allow for effective and reliable inter-study size comparisons alongside the development of a large-scale repository of chondrule size data.

Chondrule Size/Petrologic Subtype Relationship

Relationships between the size of chondrules and the extent of alteration experienced by their host meteorite/
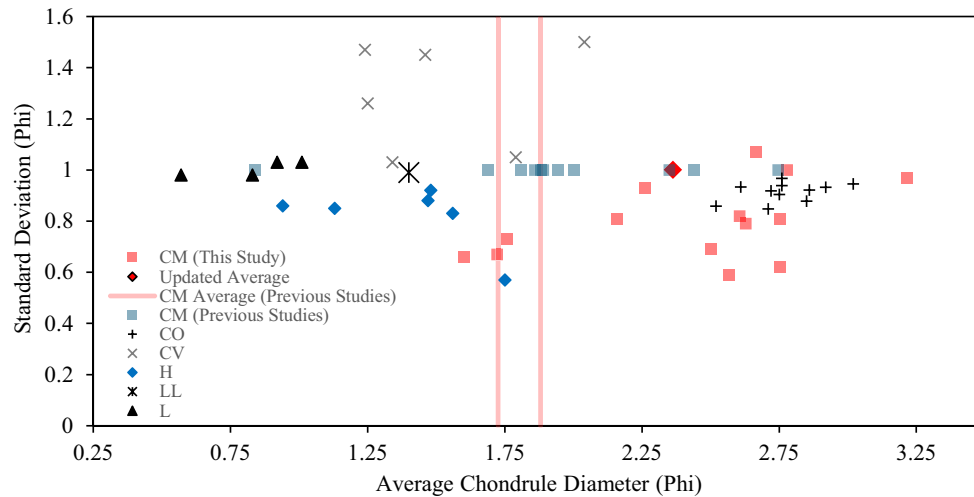
FIGURE 9. Chondrule diameters within the major chondritic groups alongside data from the present study. Data not published with graphic standard deviation were given an arbitrary standard deviation of 1 to allow useful visualization. Chondrule size averages were sourced from the following previous studies. CM chondrites: Rubin and Wasson (1986), Friend et al. (2018), Hanna and Ketcham (2018), Vacher et al. (2018), Kimura et al. (2020), Fendrich and Ebel (2021), Kerraouch et al. (2021). CO chondrites: Rubin (1989). CV chondrites: King and King (1978). H, L, and LL chondrites: King and King (1979).

lithology have been described for other carbonaceous groups including the COs where average chondrule size increases with petrologic type (Pinto et al., 2021; Rubin, 1989).

Brecciation within the CM chondrites is well recorded and considered ubiquitous within the group (Metzler et al., 1992) with clasts representing highly variable fractions of any CM chondrite volume. Differences in petrologic subtype between clasts are recorded here and within other studies (Bischoff et al., 2017; Lentfort et al., 2020; Suttle et al., 2022). The effects of brecciation and intra-meteorite lithological differences have made identifying any relationship between alteration extent and chondrule size extremely challenging within the CMs. Analysis of any correlation between chondrule size and petrologic subtype is complicated further by the wide-ranging and often overlapping parameters within the Rubin et al. (2007) and Rubin (2015) classification scheme, resulting in identical subtype classifications for clasts and lithologies which may appear very different in BSE images and EDS maps. The extent of this issue for chondrule size analysis is highlighted by the large spread of sizes recorded within the CM2.2 lithologies identified here (Average R_1: 93.51–449.1 μm).

By studying a relatively large number of samples and classifying each clast, we have been able to assign a petrologic subtype to the host lithology for all chondrules measured in 2-D, facilitating analysis of chondrule size variations between host lithology subtypes (Figure 10a). 3-D data are excluded from this analysis as subtype cannot be determined by XCT. Subsequently, clasts and lithologies with $n < 10$ chondrules were excluded to

reduce noise from small and possibly unrepresentative samples, the results are plotted in Figure 10b.

Alongside these data, CO chondrite data from studies by Ebel et al. (2016) and Pinto et al. (2021) are shown (Figure 10a,b). The methodologies used for chondrule measurements in these studies differed from the CIS methodology used here. In both studies, chondrule sizes are calculated as the diameters of circles of equivalent area, a methodology consistent with earlier CO chondrite chondrule studies (Rubin, 1989). The use of a more consistent methodology for CO chondrite chondrule measurement has allowed for better inter-study comparisons of their size. However, the finding by Rubin and Wasson (2005) that ~60% of CO chondrules have a lobate shape suggests that the area equivalent methodology applied in these chondrule size studies is likely masking the actual observed 2-D long- and short-axis sizes.

The results illustrated in Figure 10b show the 2-D measured CM chondrule sizes are generally larger than those in the CO chondrites with overlapping average sizes in some clasts/lithologies. Calculation of a weight average 2-D chondrule size shows a potential correlation between average chondrule size and petrologic subtype ($R^2 = 0.7668$). Further chondrule size data correlated with petrologic subtype for both the CM and CO chondrites are required to ascertain the full extent of any relationship with a particular focus on applying the CIS methodology to the CO chondrites.

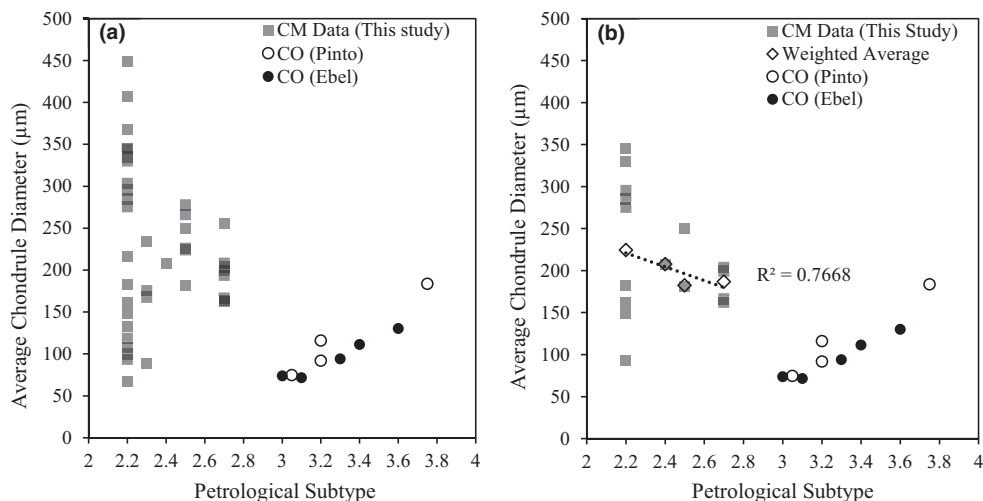Two potential explanations for a chondrule size/petrological subtype relationship within the CM's include:

FIGURE 10. Plots showing the relationship between 2-D measured average chondrule size and petrologic subtype alongside data for CO chondrule size and petrologic type. (a) All clasts/lithologies, (b) clasts or lithologies with >10 chondrules with weighted average size for each subtype.

1. Aqueous alteration selectively destroying smaller chondrules, resulting in a bias toward larger particles within more altered samples.
2. A size sorting process occurring during parent body accretion such as the contraction of a self-gravitating clump of chondrules of various sizes (Pinto et al., 2021). Such a process would produce a size gradation of chondrules within the original parent body, with larger chondrules toward its center. Subsequent aqueous alteration may then have been more intense at greater depths within the parent body as a result of proximity to decaying ^{26}Al (Kerraouch et al., 2019; Visser et al., 2020).

Assessing the likelihood of each of these scenarios, only in the most heavily altered CM chondrites is complete alteration of chondrules observed. In the case of scenario one, it would be expected that evidence for increasing chondrule alteration should be observed from mildly to moderately aqueously altered specimens. We believe the absence of such a trend precludes aqueous alteration being solely responsible for a chondrule size/petrologic subtype relationship. Furthermore, the wide variation in chondrule sizes observed in the more altered CM chondrites (CM2.2) suggests that a scenario where smaller chondrule sizes are being preferentially destroyed seems unlikely. Of the two hypothesized explanations for a potential relationship between chondrule size and petrologic subtype, we therefore favor explanation two, schematically illustrated in Figure 11. Explanation two better allows for the variability in the chondrule sizes observed and does not require evidence for chondrule alteration at lower petrologic subtypes. Further data collection and modeling are required to fully understand the extent to which explanation two

could be applicable especially with regard to better constraining an average for more altered samples (CM2.0–2.2) where a significant spread in chondrule sizes is observed.

Implications for the CM-CO Clan

The revised average size of the CM chondrite chondrules presented here has implications for the widely discussed CM-CO clan (Chaumard et al., 2018; Kallemeyn & Wasson, 1979, 1982; Rubin & Wasson, 2005; Schrader & Davidson, 2017; Weisberg et al., 2006; Zhu et al., 2021).

Previous studies have identified mineralogical and geochemical similarities (Weisberg et al., 2006), similarities in refractory lithophile abundance (Kallemeyn & Wasson, 1979), similarities in ε^{54}Cr compositions (Zhu et al., 2021), and Mg and O isotopic signatures suggesting a common chondrule origin (Chaumard et al., 2018; Schrader & Davidson, 2017) as evidence in support of the CM-CO clan and a close genetic link between the groups. However, despite the evidence presented and suggestions of single shared parent body (Greenwood et al., 2014), the true extent of the relationship between the CM and CO chondrites remains heavily debated.

In many cases, authors have used a resolvable difference in the average chondrule size between the two groups as the first line of evidence against a shared parent body or close genetic link. The reported CO chondrite average chondrule size of $148 + 132/-70\,\mu m$ (Rubin 1989). The smaller average chondrule size reported here for the CM chondrites ($194\,\mu m$) should call into question the notion that there is a significant difference in size between the CM and CO chondrules. The use of a size
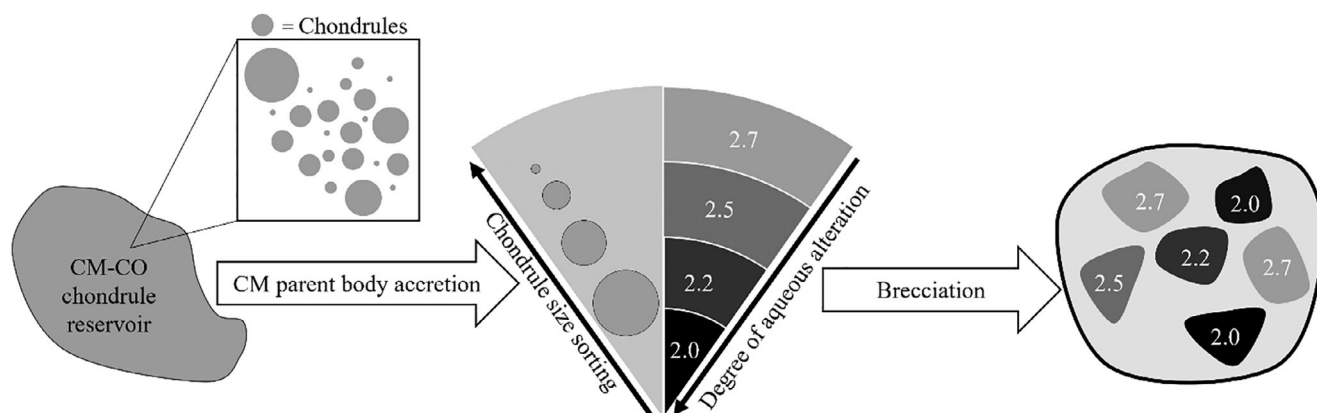
FIGURE 11. Schematic diagram outlining the series of events which could have led to the relationship between chondrule size and petrological subtype as observed within the CM chondrites.

difference between the two groups should therefore not be used as evidence against a shared parent body or genetic link.

Furthermore, the trend between chondrule size and petrologic subtype indicated in this work could further support a link between the CM and CO groups. When the CM petrological trend is compared with recent, high-resolution analyses of the CO group (Pinto et al., 2021) (Figure 10a,b), chondrule sizes appear to converge toward a more similar size at a 3.0 classification. This convergence provides yet further evidence for a deeply intertwined history between the CM and CO chondrites. While differences between the two groups remain (e.g., chondrule and matrix abundances, cosmic ray exposure ages and the lack of brecciation in the CO chondrites; Eugster, 2003), the findings presented here show that differences in chondrules size should not be used as evidence against the CM-CO clan. Instead, the similarity in chondrule sizes between the groups strengthens evidence for the strong affinity between the CM-CO chondrites and their likely similar early histories.

CONCLUSIONS

The findings presented here show that the commonly cited literature value for the CM chondrite chondrule size is overstated, likely as a consequence of the measurement methods used. An updated average chondrule size based on our results, and which aligns better with other recent CM studies, of 2.363ϕ (194 μm) is proposed. It is also recommended that the CIS methodology be adopted as a standardized approach to chondrule size measurements to help improve inter-study comparisons of chondrule size. We also support the recommendations of other authors that undigested (raw) chondrule size data should be presented alongside average chondrule size values, and data from this study can be found in Material S1 (Friedrich et al., 2015).

Additionally, the methods used here have demonstrated the significance of resolution when quantifying particle size. This is most important when using 3-D techniques such as XCT where resolutions may be poorer owing to limitations in scanning large chips. The application of robust stereological corrections to CM chondrules remains a challenge due to their non-spherical form; however, the results here indicate that application of the model developed by Benito et al. (2019) provides the best estimate for a 3-D particle size distribution.

Data Availability Statement—The data that supports the findings of this study are available in the supplementary material of this article.

Editorial Handling—Dr. Akira Yamaguchi

REFERENCES

Benito, S., Cuervo, C., Pöhl, F., and Theisen, W. 2019. Improvements on the Recovery of 3D Particle Size Distributions from 2D Sections. *Materials Characterization* 156: 109872.

Bischoff, A., Ebert, S., Metzler, K., and Lentfort, S. 2017. Breccia classification of CM chondrites (abstract). *Meteoritics and Planetary Science* 52: 6089.

Bischoff, A., Scott, E. R. D., Metzler, K., and Goodrich, C. A. 2006. Nature and origins of meteoritic breccias. In *Meteorites and the early solar system II*, edited by D. S. Lauretta, and H. Y. McSween, 679–712. Tucson: University of Arizona Press.

Blott, S. J., and Pye, K. 2001. Gradistat: A Grain Size Distribution and Statistics Package for the Analysis of Unconsolidated Sediments. *Earth Surface Processes and Landforms* 26: 1237–48.

Charles, C. R. J., Robin, P. Y. F., Davis, D. W., and McCausland, P. J. A. 2018. Shapes of Chondrules Determined from the Petrofabric of the CR2 Chondrite NWA 801. *Meteoritics & Planetary Science* 53: 935–951.

Chaumard, N., Defouilloy, C., and Kita, N. T. 2018. Oxygen Isotope Systematics of Chondrules in the Murchison CM2 chondrite and Implications for the CO-CM Relationship. *Geochimica et Cosmochimica Acta* 228: 220–242.

Choe, W. H., Huber, H., Rubin, A. E., Kallemeyn, G. W., and Wasson, J. T. 2010. Compositions and Taxonomy of 15 Unusual Carbonaceous Chondrites. *Meteoritics & Planetary Science* 45: 531–554.

Connolly, H. C., and Jones, R. H. 2016. Chondrules: The Canonical and Noncanonical Views. *Journal of Geophysical Research: Planets* 121: 1885–99.

Cuzzi, J. N., Hogan, R. C., Paque, J. M., and Dobrovolskis, A. R. 2001. Size-Selective Concentration of Chondrules and Other Small Particles in Protoplanetary Nebula Turbulence. *The Astrophysical Journal* 546: 496–508.

Cuzzi, J. N., and Olson, D. M. 2017. Recovering 3D Particle Size Distributions from 2D Sections. *Meteoritics & Planetary Science* 52: 532–545.

Dodd, R. T. 1982. Objects we Call Chondrules. In *Chondrules and their Origins*, 15. Houston, TX: Lunar and Planetary Institute.

Ebel, D. S., Brunner, C., Konrad, K., Leftwich, K., Erb, I., Lu, M., Rodriguez, H., Crapster-Pregont, E. J., Friedrich, J. M., and Weisberg, M. K. 2016. Abundance, Major Element Composition and Size of Components and Matrix in CV, CO and Acfer 094 Chondrites. *Geochimica et Cosmochimica Acta* 172: 322–356.

Eisenhour, D. D. 1996. Determining Chondrule Size Distributions from Thin-Section Measurements. *Meteoritics & Planetary Science* 31: 243–48.

Eugster, O. 2003. Cosmic-Ray Exposure Ages of Meteorites and Lunar Rocks and their Significance. *Geochemistry* 63: 3–30.

Fan, Y., Li, S., Liu, S., Yin, Q., Song, G., Xu, R., Zhang, J., et al. 2022. Shidian Meteorite, a New Fall Analog of near-Earth Asteroid (101955) Bennu. *Meteoritics & Planetary Science* 57: 2192–2215.

Fendrich, K. V., and Ebel, D. S. 2021. Comparison of the Murchison CM2 and Allende CV3 Chondrites. *Meteoritics & Planetary Science* 56: 77–95.

Floyd, C. J., and Lee, M. R. 2022. The CIS Method: A Proposed Standardised Protocol for Measuring and Reporting Sizes of Chondrules and Other Chondritic Objects (Abstract #6087). 85th Annual Meeting of the Meteoritical Society.

Folk, R. L., and Ward, W. C. 1957. Brazos River Bar [Texas]: A Study in the Significance of Grain Size Parameters. *Journal of Sedimentary Research* 27: 3–26.

Friedrich, J. M., Weisberg, M. K., Ebel, D. S., Biltz, A. E., Corbett, B. M., Iotzov, I. V., Khan, W. S., and Wolman, M. D. 2015. Chondrule Size and Related Physical Properties: A Compilation and Evaluation of Current Data across all Meteorite Groups. *Geochemistry* 75: 419–443.

Friend, P., Hezel, D. C., Barrat, J. A., Zipfel, J., Palme, H., and Metzler, K. 2018. Composition, Petrology, and Chondrule-Matrix Complementarity of the Recently Discovered Jbilet Winselwan CM2 Chondrite. *Meteoritics & Planetary Science* 53: 2470–91.

Greenwood, R. C., Howard, K. T., Fran-Chi, I. A., Zolensky, M. E., Buchanan, P. C., and Gibson, J. M. 2014. Oxygen Isotope Evidence for the Relationship between CM and CO Chondrites: Could they both Coexist on a Single Asteroid? *45th Lunar and Planetary Science Conference* (abstract #2610).

Hamilton, V. E., Simon, A. A., Christensen, P. R., Reuter, D. C., Clark, B. E., Barucci, M. A., Bowles, N. E., et al. 2019. Evidence for Widespread Hydrated Minerals on Asteroid (101955) Bennu. *Nature Astronomy* 3: 332–340. http://www.nature.com/articles/s41550-019-0722-2.

Hanna, R. D., and Ketcham, R. A. 2018. Evidence for Accretion of Fine-Grained Rims in a Turbulent Nebula for CM Murchison. *Earth and Planetary Science Letters* 481: 201–211.

Hanna, R. D., Ketcham, R. A., Zolensky, M., and Behr, W. M. 2015. Impact-Induced Brittle Deformation, Porosity Loss, and Aqueous Alteration in the Murchison CM Chondrite. *Geochimica et Cosmochimica Acta* 171: 256–282. https://doi.org/10.1016/j.gca.2015.09.005.

Hewins, R. H. 1997. Chondrules. *Annual Review of Earth and Planetary Sciences* 25: 61–83.

Hewins, R. H., Bourot-Denise, M., Zanda, B., Leroux, H., Barrat, J. A., Humayun, M., Göpel, C., et al. 2014. The Paris Meteorite, the least Altered CM Chondrite So Far. *Geochimica et Cosmochimica Acta* 124: 190–222.

Howard, K. T., Alexander, C. M. O., Schrader, D. L., and Dyl, K. A. 2015. Classification of Hydrous Meteorites (CR, CM and C2 Ungrouped) by Phyllosilicate Fraction: PSD-XRD Modal Mineralogy and Planetesimal Environments. *Geochimica et Cosmochimica Acta* 149: 206–222.

Jarosewich, E. 1990. Chemical Analyses of Meteorites: A Compilation of Stony and Iron Meteorite Analyses. *Meteoritics* 25: 323–337.

Jones, R. H., Lee, T., Connolly, H. C., Jr., Love, S. G., and Shang, H. 2000. Formation of chondrules and CAIs: Theory VS. observation. In *Protostars and planets IV*, edited by V. Manning, A. P. Boss, and S. S. Russel, 927–962. Tucson: University of Arizona Press.

Kallemeyn, G. W., and Wasson, J. T. 1979. Refractory Element Fractionations among Carbonaceous Chondrite Groups [11]. *Nature* 282: 827–29.

Kallemeyn, G. W., and Wasson, J. T. 1982. The Compositional Classification of Chondrites: III. Ungrouped Carbonaceous Chondrites. *Geochimica et Cosmochimica Acta* 46: 2217–28.

Kerraouch, I., Bischoff, A., Zolensky, M. E., Pack, A., Patzek, M., Hanna, R. D., Fries, M. D., et al. 2021. The Polymict Carbonaceous Breccia Aguas Zarcas: A Potential Analog to Samples Being Returned by the OSIRIS-REx and Hayabusa2 Missions. *Meteoritics & Planetary Science* 56: 277–310.

Kerraouch, I., Ebert, S., Patzek, M., Bischoff, A., Zolensky, M. E., Pack, A., Schmitt-Kopplin, P., Belhai, D., Bendaoud, A., and Le, L. 2019. A Light, Chondritic Xenolith in the Murchison (CM) Chondrite—Formation by Fluid-Assisted Percolation during Metasomatism? *Chemie der Erde* 79: 125518.

Ketcham, R. A. 2005. Computational Methods for Quantitative Analysis of Three-Dimensional Features in Geological Specimens. *Geosphere* 1: 32–41.

Kimura, M., Imae, N., Komatsu, M., Barrat, J. A., Greenwood, R. C., Yamaguchi, A., and Noguchi, T. 2020. The most Primitive CM Chondrites, Asuka 12085, 12169, and 12236, of Subtypes 3.0–2.8: Their Characteristic Features and Classification. *Polar Science* 26: 100565.

King, A. J., Bates, H. C., Schofield, P. F., and Russell, S. S. 2021. The bulk mineralogy A and water contents of the carbonaceous chondrite falls Kolang and Tarda. *52nd Lunar and Planetary Science Conference*, abstract#1909.

King, A. J., Daly, L., Rowe, J., Joy, K. H., Greenwood, R. C., Devillepoix, H. A. R., Suttle, M. D., Chan, Q. H. S., et al. 2022. The Winchcombe Meteorite, a Unique and Pristine Witness from the Outer Solar System. *Science Advances* 8: eabq3925.

King, T. V. V., and King, E. A. 1978. Grain Size and Petrography of C2 and C3 Carbonaceous Chondrites. *Meteoritics* 13: 47–72.

King, T. V. V., and King, E. A. 1979. Size Frequency Distributions of Fluid Drop Chondrules in Ordinary Chondrites. *Meteoritics* 14: 91–96.

Krot, A. N., Keil, K., Scott, E. R. D., Goodrich, C. A., and Weisberg, M. K. 2014. Classification of meteorites and their genetic relationships. In *Treatise on geochemistry*, edited by H. D. Holland, and K. K. Turekian, 2nd ed., vol. 1, 1–63. Elsevier.

Krumbein, W. C. 1936. Application of Logarithmic Moments to Size Frequency Distributions of Sediments. *SEPM Journal of Sedimentary Research* 6: 35–47.

Lee, M. R., Cohen, B. E., King, A. J., and Greenwood, R. C. 2019. The Diversity of CM Carbonaceous Chondrite Parent Bodies Explored Using Lewis Cliff 85311. *Geochimica et Cosmochimica Acta* 264: 224–244.

Lee, M. R., Floyd, C., Martin, P. E., Zhao, X., Franchi, I. A., Jenkins, L., and Griffin, S. 2023. Extended Time Scales of Carbonaceous Chondrite Aqueous Alteration Evidenced by a Xenolith in LaPaz Icefield 02239 (CM2). *Meteoritics & Planetary Science* 58: 672–687.

Lentfort, S., Bischoff, A., Ebert, S., and Patzek, M. 2020. Classification of CM Chondrite Breccias—Implications for the Evaluation of Samples from the OSIRIS-REx and Hayabusa 2 Missions. *Meteoritics & Planetary Science* 21: 1–21.

Lindgren, P., Hanna, R. D., Dobson, K. J., Tomkinson, T., and Lee, M. R. 2015. The Paradox between Low Shock-Stage and Evidence for Compaction in CM Carbonaceous Chondrites Explained by Multiple Low-Intensity Impacts. *Geochimica et Cosmochimica Acta* 148: 159–178.

Metzler, K. 2004. Formation of Accretionary Dust Mantles in the Solar Nebula: Evidence from Preirradiated Olivines

in CM Chondrites. *Meteoritics & Planetary Science* 39: 1307–19.

Metzler, K. 2018. From 2D to 3D Chondrule Size Data: Some Empirical Ground Truths. *Meteoritics & Planetary Science* 53: 1489–99.

Metzler, K., Bischoff, A., and Stöffler, D. 1992. Accretionary Dust Mantles in CM Chondrites: Evidence for Solar Nebula Processes. *Geochimica et Cosmochimica Acta* 56: 2873–97.

Miura, H., Nakamoto, T., and Doi, M. 2008. Origin of Three-Dimensional Shapes of Chondrules: I. Hydrodynamics Simulations of Rotating Droplet Exposed to High-Velocity Rarefied Gas Flow. *Icarus* 197: 269–281.

Oakeshott, R. B. S., and Edwards, S. F. 1992. On the Stereology of Ellipsoids and Cylinders. *Physica A: Statistical Mechanics and its Applications* 189: 208–233.

Pinto, G. A., Marrocchi, Y., Morbidelli, A., Charnoz, S., Eugenia, V. M., Soto, K., Martínez, R., and Olivares, F. 2021. Constraints on Planetesimal Accretion Inferred from Particle-Size Distribution in CO Chondrites. *The Astrophysical Journal Letters* 917: L25.

Rubin, A. E. 1989. Size-Frequency Distributions of Chondrules in CO3 Chondrites. *Meteoritics* 24: 179–189.

Rubin, A. E. 2012. Collisional Facilitation of Aqueous Alteration of CM and CV Carbonaceous Chondrites. *Geochimica et Cosmochimica Acta* 90: 181–194.

Rubin, A. E. 2015. An American on Paris: Extent of Aqueous Alteration of a CM Chondrite and the Petrography of its Refractory and Amoeboid Olivine Inclusions. *Meteoritics & Planetary Science* 50: 1595–1612.

Rubin, A. E., Trigo-Rodríguez, J. M., Huber, H., and Wasson, J. T. 2007. Progressive Aqueous Alteration of CM Carbonaceous Chondrites. *Geochimica et Cosmochimica Acta* 71: 2361–82.

Rubin, A. E., and Wasson, J. T. 1986. Chondrules in the Murray CM2 meteorite and Compositional Differences between CM-CO and Ordinary Chondrite Chondrules. *Geochimica et Cosmochimica Acta* 50: 307–315.

Rubin, A. E., and Wasson, J. T. 2005. Non-spherical Lobate Chondrules in CO3.0 Y-81020: General Implications for the Formation of Low-FeO Porphyritic Chondrules in CO Chondrites. *Geochimica et Cosmochimica Acta* 69: 211–220.

Sahagian, D. L., and Proussevitch, A. A. 1998. 3D Particle Size Distributions from 2D Observations: Stereology for Natural Applications. *Journal of Volcanology and Geothermal Research* 84: 173–196.

Schindelin, J., Arganda-Carreras, I., Frise, E., Kaynig, V., Longair, M., Pietzsch, T., Preibisch, S., et al. 2012. Fiji: An Open-Source Platform for Biological-Image Analysis. *Nature Methods* 9: 676–682. https://www.nature.com/articles/nmeth.2019.

Schrader, D. L., and Davidson, J. 2017. CM and CO Chondrites: A Common Parent Body or Asteroidal Neighbors? Insights from Chondrule Silicates. *Geochimica et Cosmochimica Acta* 214: 157–171.

Scott, E. R. D., and Krot, A. N. 2013. Chondrites and their components. In *Treatise on geochemistry*, edited by H. D. Holland, and K. K. Turekian, 2nd ed., 65–137. Elsevier.

Suttle, M. D., Daly, L., Jones, R. H., Jenkins, L., van Ginneken, M., Mitchell, J. T., Bridges, J. C., et al. 2022. The Winchcombe Meteorite—A Regolith Breccia from a Rubble Pile CM Chondrite Asteroid. *Meteoritics & Planetary Science* 59: 1043–67.

Teitler, S. A., Paque, J. M., Cuzzi, J. N., and Hogan, R. C. 2011. Statistical Tests of Chondrule Sorting.

Tsuchiyama, A., Shigeyoshi, R., Kawabata, T., Nakano, T., Uesugi, K., and Shirono, S. 2003. Three-Dimensional Structures of Chondrules and their High-Speed Rotation. *34th Lunar and Planetary Science Conference*, abstract #1271.

Vacher, L. G., Marrocchi, Y., Villeneuve, J., Verdier-Paoletti, M. J., and Gounelle, M. 2018. Collisional and Alteration History of the CM Parent Body. *Geochimica et Cosmochimica Acta* 239: 213–234.

Visser, R., John, T., Whitehouse, M. J., Patzek, M., and Bischoff, A. 2020. A Short-Lived 26Al Induced Hydrothermal Alteration Event in the Outer Solar System: Constraints from Mn/Cr Ages of Carbonates. *Earth and Planetary Science Letters* 547: 116440.

Weisberg, M. K., McCoy, T. J., and Krot, A. N. 2006. Systematics and evaluation of meteorite classification. In *Meteorites and the early solar system II*, edited by D. S. Lauretta, and H. Y. McSween, 19–52. Tucson: University of Arizona Press.

Wlotzka, F. 1983. Composition of chondrules, fragments and matrix in the unequilibrated ordinary chondrites tieschitz and sharps. In *Chondrules and their origins*, edited by E. A. King, 296–318. Houston: Lunar and Planetary Institute.

Wurm, G., Teiser, J., Bischoff, A., Haack, H., and Roszjar, J. 2010. Experiments on the Photophoretic Motion of Chondrules and Dust Aggregates-Indications for the Transport of Matter in Protoplanetary Disks. *Icarus* 208: 482–491.

Zanda, B. 2004. Chondrules. *Earth and Planetary Science Letters* 224: 1–17.

Zhu, K., Moynier, F., Schiller, M., Alexander, C. M. O. D., Davidson, J., Schrader, D. L., van Kooten, E., and Bizzarro, M. 2021. Chromium Isotopic Insights into the Origin of Chondrite Parent Bodies and the Early Terrestrial Volatile Depletion. *Geochimica et Cosmochimica Acta* 301: 158–186.

SUPPORTING INFORMATION

Additional supporting information may be found in the online version of this article.

Figure S1. Graph showing the relationship between weighted average chondrule long axis length and petrologic subtype.

Data S1. Raw 2D and 3D chondrule size data for all chondrules measured.